



Contents lists available at ScienceDirect

Journal of Fluids and Structures

journal homepage: www.elsevier.com/locate/jfs

Analysis of tidal turbine blade loading due to blade scale flow

H. Mullings*, T. Stallard

School of Engineering, The University of Manchester, Manchester, United Kingdom



ARTICLE INFO

Article history:

Received 22 December 2021

Received in revised form 6 May 2022

Accepted 25 July 2022

Available online 23 August 2022

Keywords:

Tidal turbine

Fatigue

Turbulence

Blade scale

ABSTRACT

A blade element model is developed to include unsteady lift and drag coefficients and it is shown that this provides improved prediction of the spectrum of root bending moment of a tidal turbine blade for two definitions of onset turbulence. Computational Fluid Dynamics (CFD) is used to model the lift and drag forces on a 2D aerofoil using the relative onset flow from the different turbulence generation methods. Inclusion of the magnitude of high frequency fluctuations within the blade load spectra, results in an increased number of load cycles and improves prediction of Damage Equivalent Load (DEL). Discrepancy between prediction and existing experimental data is improved from 15% to within 2%. The signal-to-noise ratio (SNR) of relative velocity has been used to characterise the onset flow, and a relationship is established between onset flow conditions and the resultant fatigue loads (DEL). This has been applied to a number of onset conditions, typical of channel shear flows and upstream turbine wakes. For a given SNR, there is a 3.3 factor of variation in the DEL across the range of tip-speed-ratio (TSR) shown and over a single TSR value there is a 6.5 factor of variation across the DEL, over the largest range of SNR.

© 2022 The Author(s). Published by Elsevier Ltd. This is an open access article under the CC BY license (<http://creativecommons.org/licenses/by/4.0/>).

1. Introduction

Tidal turbines have proven they can be used for energy generation through full scale testing (Parkinson and Collier, 2016; McNaughton et al., 2015) and small array deployments (IMechE, 2020). The success of these deployments depends upon the availability of the devices, as a measure of the potential power which can be generated. For wind turbines this measure has a range of uses, it can be used to determine energy estimates, evaluate performance and predict revenue (DNV GL, 2017). Therefore, it is important to investigate any factors which can influence this measure. A key factor which contributes to the availability is the reliability of the device. A turbine's reliability is dependent upon the design life of the individual components. These components undergo differing conditions based on their location at the site. Extensive work has been conducted by The University of Exeter (Weller et al., 2017; Thies et al., 2015) examining the methods that can be used to calculate the reliability for mooring lines and power cables. The focus of this work is on the reliability of the blades, this is a component of the turbine which experienced the most failures in deployment (Walker and Thies, 2021). These failures were either due to defects from the manufacturing process, or the blades experiencing higher loading than expected. The loads that the blades experience can be predicted using a Blade Element Momentum (BEM) theory (Togneri et al., 2020; Parkinson and Collier, 2016) or more detailed Computational Fluid Dynamics (CFD) models (Afgan et al., 2013; Ahmed et al., 2017). The drawback of CFD models is the computational cost, with fully blade resolved models requiring supercomputer access to run for one design case. Steady loading cases are quick to calculate using BEM methods, with

* Corresponding author.

E-mail addresses: hannah.mullings@manchester.ac.uk (H. Mullings), tim.stallard@manchester.ac.uk (T. Stallard).

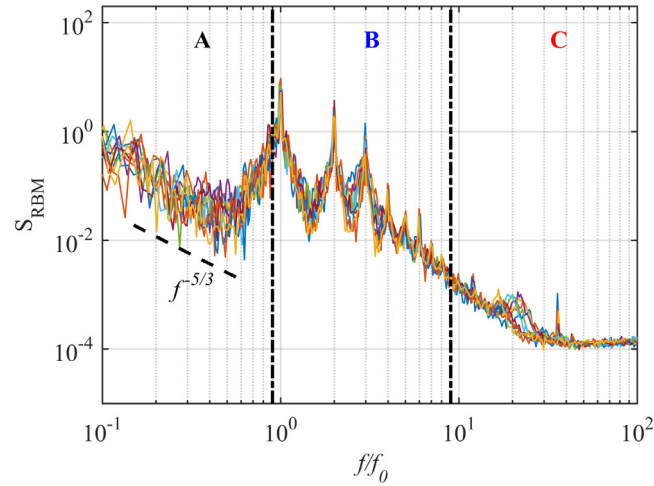


Fig. 1. Experimental blade loading spectra, with sections defined for different frequency ranges of interest.

more detailed simulations possible with the combination of BEM with CFD, combining a Reynolds Averaged Navier–Stokes (RANS) simulation with BEM (Olczak et al., 2016). Unsteady blade loading without a fully resolved model is possible using Actuator Line (AL) models (Ouro et al., 2017; Apsley and Stansby, 2020). When assessing multiple operational conditions for unsteady loading a combination of Blade Element theory (BE) with synthetic turbulence inflow is shown to provide close prediction of loads against experimental data (Mullings and Stallard, 2018).

Accurate prediction of onset flow and resultant turbine loading is required for the assessment of component fatigue life. The variation of onset flow characteristics, caused by different environmental factors, can include a range of flow speeds and profiles as well as a change in turbulence parameters, such as intensity and length-scale. Each individual turbine will be affected by the onset flow, however if there is a large array then each turbine will also have the effects of blockage and wakes between the turbines. By understanding the different loading patterns, more accurate design life can be estimated along with overall performance, which leads to the motivation behind this work. The aim of this paper is to assess the additional influence of blade scale flow through the impact of the unsteady onset flow on the lift and drag forces, onto the predicted blade loads.

2. Motivation

The unsteady loads that a tidal turbine experiences during operation will affect the overall time that the turbine will generate power as designed. Current full scale developments are planning for a blade lifetime of 6 years (Atlantis, 2018), with a triple redundancy built in. Due to the location and nature of the turbine, it experiences time-varying cyclic loading. The main variability in the loads is caused around the rotational frequency of the rotor by hostile environmental conditions such as velocity shear, waves and turbulence. To study the influence of these conditions on the design life of turbine components, a single turbine is considered. There are different load modelling approaches available, which range from CFD, which involves either fully blade resolved geometry (Ahmed et al., 2017) or actuator lines (Apsley et al., 2018; Ouro et al., 2017). The disadvantage of these methods is the computational time and resources required to simulate only one operational point, which can require days of simulation time. A simpler method is to employ a BEM method which has a low computational cost and is employed within industry software, such as Tidal Bladed. Traditionally, BEM is used to determine the loading using steady inflow conditions, however, work has been conducted by Togneri et al. (2011) to develop a BEMT model which accounts for the variation in turbulence due to characteristics found at specific full scale sites. Work conducted as part of the ReDAPT project (Reliable Data Acquisition Platform for Tidal) (Ahmed et al., 2017) found that fluctuations in load on a single blade have multiple sources; tower shadow, velocity shear, ambient turbulence and blade-generated turbulence.

Fig. 1 is included to highlight the frequency ranges which these sources affect. Section A contains low frequency fluctuations which are due to turbulence and hence follow the energy decay specified by Kolmogorov ($f^{-5/3}$) (Kolmogorov et al., 1991). Section B is the mid frequency range which also follows the energy decay from turbulent eddies, but also includes peaks at frequencies corresponding to the rotor harmonics and blade passing frequency. Section C corresponds to the high frequency fluctuations and experimental noise is a large contributor to the magnitude of the fluctuations within this frequency range. It was also established in Ahmed et al. (2017) that there is an increase in gradient due to blade scale fluctuations which is detected using a fully blade resolved CFD model.

The effect on fatigue loading on a turbine blade due to a range of environmental conditions is investigated, with an emphasis on how the onset flow conditions are characterised to induce the blade scale fluctuations of loads that dominate in the high frequency range.

3. Method

The loading response using a modified BEMT model is explored using alternative synthetic turbulence models for the inflow. The power density spectra of the loading for the different flow fields is compared, highlighting the decrease in spectral magnitude over the mid to high frequency range ($> 10f_0$). This decrease in spectral variation is caused by the coherency of the turbulent structures, especially when using the Synthetic Eddy Method (SEM). One method for mitigating this is used in [Togneri et al. \(2020\)](#), where length scales are distributed with standard deviations between 25% to 75%. This method results in an increase in the spectral variation over the mid frequency range, however, this has not been shown over the whole frequency range with confidence. This study focuses on prediction of the full spectra of blade loading, with validation relative experimental results, by utilising an efficient blade element method. The purpose is to establish fatigue load by varying the turbine operating point, as well as characterising the influence of deterministic loading factors on the fatigue.

3.1. Onset flow modelling

The work in this study utilises two different turbulence models. The first is the von Kármán method, this uses a random statistical approach to model combined stochastic velocity spectra. The second method is the SEM, originally created by [Jarrin et al. \(2006\)](#) for use as inflow to LES simulations. This method uses a stochastic algorithm to generate instantaneous velocity fluctuations. Both methods rely on knowledge of specific turbulence parameters, such as turbulence intensity (TI) and lengthscale (ℓ_x), as described by Eqs. (1)–(2).

$$TI = \frac{u'}{U} \quad (1)$$

Where u' is the variance of the velocity fluctuations and U is the mean onset velocity.

$$\ell_x = U_0 \int_0^\infty R_N(t) dt \quad (2)$$

Where ℓ_x is the streamwise lengthscale, U_0 is the onset flow velocity and R_N is the auto-correlation function with respect to time.

For this case the parameters used correspond to the conditions at an experimental test facility as these results will be used for comparison. The experimental results were obtained as part of the X-MED project, which created a 1.2 m bed-mounted turbine, as described in [Payne et al. \(2018\)](#). The testing facility used was IFREMER in Bologne-Sur-Mer, and the tank specification is given in detail in [Gaurier et al. \(2013\)](#). The turbulence characteristics considered here are as described for the low turbulence case in [Payne et al. \(2017\)](#) with 3% turbulence intensity and longitudinal length scale of 0.6 m. More recent analysis of the turbulence characteristics of flow in the IFREMER flume are given in [Slama et al. \(2021\)](#). These two methods create frozen turbulence fields which are used to define the inflow to the turbine. The turbulence characteristics are calculated with both cases having a matching intensity of 3% and calculated lengthscales within 10% for the von Kármán method and 19% for the SEM. These turbulent inflows form the basis for the loading calculations. In reality, turbines will experience a range of operational conditions which will influence the magnitude of the loading. The influence of these conditions is investigated here through an examination of the magnitude of periodic components and the background noise. The periodic variations are considered deterministic as they are caused by the rotation of the turbine through steady conditions such as shear. The background noise within the onset flow is caused by the stochastic occurrence of turbulence. As the turbulence is generated using two differing methods, the noise produced within the load spectra differs. In order to investigate the noise, the spectra of the onset relative velocity at a blade segment is examined. The relationship between the deterministic and stochastic components within the onset flow conditions has been defined through a signal-to-noise ratio (SNR). Widely used in acoustics, the SNR defines how strong the signal is compared to the background noise.

The magnitude of the signal and noise is calculated using the relative onset flow to the blade at radius $r = 0.7R$. The spectra of both the onset flow at this blade position and the relative onset flow, with no added periodic components, is shown in [Fig. 2](#). On examination, the onset flow at the blade from each generation method results in a different spectra, with the SEM case showing higher magnitude at the low frequency and much lower magnitude in the high frequency. For the spectra of relative velocity experienced at 0.7R, the von Kármán onset turbulence reproduces a similar spectral shape, showing a $-5/3$ decay of energy. For the SEM case the relative velocity spectra results in a spiked spectra with peaks corresponding to the rotational frequency and its harmonics. This is an artefact of the isotropic SEM generation and has been shown to be removed in cases with varying eddy shapes ([Togneri et al., 2020](#)). With respect to the synthetic eddy method further work has shown that there is a linear relationship between the defined characteristic length in SEM and the turbulent length scales ([Choma Bex et al., 2020](#)), allowing for scaling of the length scales, this scaling is not used in this work, as the purpose to create turbulent onset flow with two generation methods based on the same parameters.

In order to determine the SNR for each generation method the relative onset flow is filtered to separate the different components, according to Eq. (3).

$$u = \bar{u} + u' + \tilde{u} \quad (3)$$

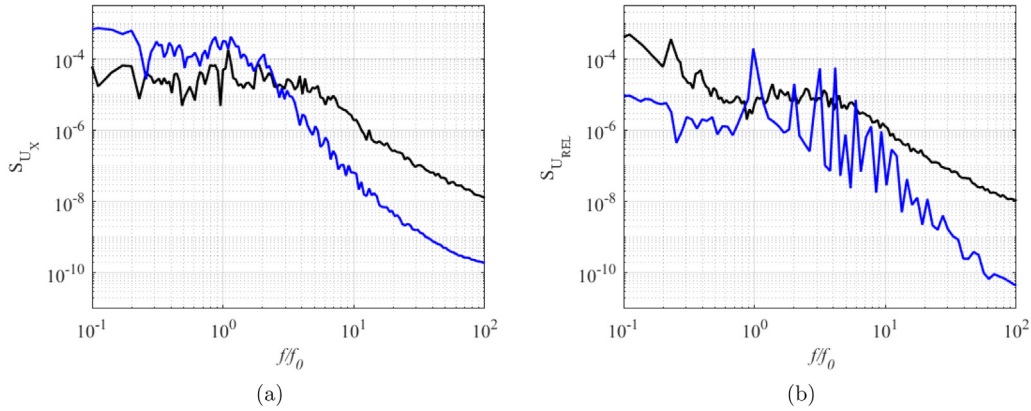


Fig. 2. Power spectra of (a) stream-wise onset flow (U_x) and (b) relative onset flow (U_{REL}) at a 0.7R blade position, extracted through the von Kármán flow field (black) and the SEM flow field (blue) at a TSR of 5.89. (For interpretation of the references to colour in this figure legend, the reader is referred to the web version of this article.)

Where \bar{u} is the mean relative onset velocity, u' is the fluctuating, turbulent component and \tilde{u} is the periodic component.

The power of the signal is calculated using the power in the filtered periodic component, and the magnitude of the turbulent component is calculated using the variance of the filtered out turbulence, with the ratio determined using Eq. (4).

$$SNR = \frac{P_{signal}}{\sigma^2(u')} \quad (4)$$

Where P_{signal} is the power in the signal from the onset relative velocity and $\sigma^2(u')$ is the variance of the turbulent component. The same method of filtering is applied to both turbulence generation methods, using a low-pass sixth order Butterworth filter with a cut-off frequency of $10f_0$, the peak magnitude of the resultant signal is considered over the first two harmonics, shown in the grey band in Fig. 3 and the turbulent component is considered as the filtered out component. The magnitude of P_{signal} is then determined using the remaining filtered PSD of U_{rel} applying the bandpower function through MATLAB to determine the power in the remaining spectra over the specified frequencies ($\pm 5\% f_{0,1}$). Characterising the onset flow by the SNR of relative velocity provides a way of comparing turbine loading in a wide range of onset conditions, which may differ in terms of vertical or transverse shear and turbulence parameters. For this work the range of SNR values have been determined based upon predefined vertical and transverse shear for one turbulence generation method, as well as the variation of SNR with the operating point of the turbine.

The operating point is varied through the rotational speed of the turbine, with the relative velocity extracted at different positions with each time step within the turbulent domain. For a given onset flow, higher values of turbine speed, hence higher tip-speed ratio, increase the signal observed by the turbine, compared to a turbine rotating at a slower speed. Transverse and vertical shear will have the largest impact on the power of the periodic component of the signal compared to the noise magnitude. This is because the onset flow to the blade is directly affected at the rotational speed of the turbine, whereas the noise component affects every position of the blade's rotation. The calculated ratios for each operational condition are compared between the turbulence generation methods. By using the same filtering technique for both methods, and an examination of previous results (Mullings and Stallard, 2019), it is expected that there will be a reduction in the power of the noise component for the SEM generation case, due to the lack of magnitude in the mid/high frequency range, which shows more coherency in the flow field.

Within the SNR value the dominant component of interest for these cases is the signal, as the background turbulence noise is generated using the same turbulence characteristics for each case. With the signal component defined by the shear, multiple cases of vertical and transverse shear have been evaluated. Vertical shear profiles are calculated using a range of power law profiles, which have been observed at tidal sites and the applied transverse profiles account for varying velocity deficit due to upstream turbine wakes. These vertical onset profiles are applied to the domain of generated turbulence as a constant across the transverse direction. The transverse shear profiles are described by velocity deficits, which are kept constant across the vertical domain. The velocity deficit from a wake is calculated using Eqs. (5)–(7). This set of Equations defines the self-similar wake profile which is outlined in Stallard et al. (2013). The rate of recovery of the velocity deficit is given in Eq. (5).

$$\frac{\Delta U_{max}}{U_0} = 0.864(X/D)^{-1/2} - 0.126 \quad (5)$$

Where the maximum velocity deficit at the centre-line of the wake is defined by ΔU_{max} , X is the downstream distance, D is the turbine diameter and U_0 is the mean onset flow. The wake half width ($y_{1/2}$) is defined as the distance to the

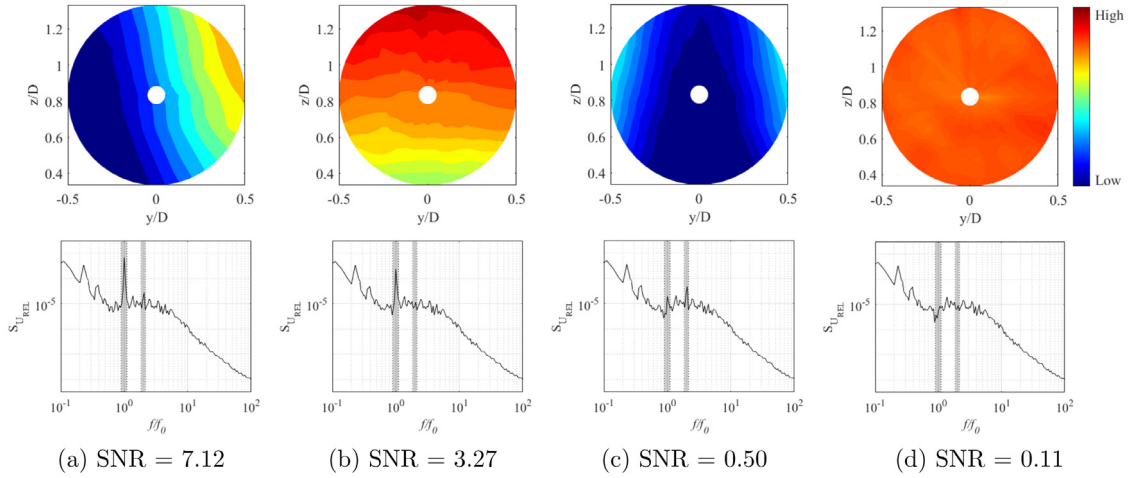


Fig. 3. Examples of different onset flow cases at one moment in time, low to high velocity as blue to red, respectively, shown by the colour scale. With the corresponding relative velocity spectra, which give SNR values from high (a) to low (d), corresponding to half a diameter offset wake at 2 diameters downstream, a vertical shear with a power law index of $1/5^{th}$, a fully inline wake and for no vertical shear or wake deficit. (For interpretation of the references to colour in this figure legend, the reader is referred to the web version of this article.)

centre-line of the wake, from a position where the deficit is half the maximum deficit, defined using Eq. (6).

$$y_{1/2} = 0.412(X/D)^{1/2} + 0.5 \quad (6)$$

The transverse velocity deficit is defined by ΔU using Eq. (7).

$$\frac{\Delta U}{\Delta U_{max}} = \exp\left(-\ln(2) \frac{y^2}{y_{1/2}^2}\right) \quad (7)$$

For differing downstream distance to a second turbine the velocity deficit changes, with the largest deficit occurring with a 2 diameter spacing (2D). Fig. 3 shows the variation in onset flow onto the turbine and the respective spectra for relative velocity at 0.7R, with the von Kármán turbulence only spectra, given by Fig. 3(d), consistent with the earlier spectra shown in Fig. 2(b). The onset flow cases shown in Fig. 3 represent the maximum wake deficit (2D) and the maximum index for the vertical power law profile and combinations. The grey banding shown across all the relative velocity spectra, highlights the regions in which the power of the signal is investigated. With these spectra corresponding to the von Kármán turbulence field, the signal peaks due to the onset conditions are clearly shown. The SNR values for these are given, with the lowest corresponding to the turbulence only case and the highest, for the offset 2D wake, where the turbine experiences the greatest variation in onset flow.

3.2. Establishing the load spectra

After determining the inflow to the turbine using a turbulent domain, and any additional onset flow conditions, the loading can be established. The method employed here extracts the onset flow at N positions along a blade length, which rotate with time, depending on the chosen operating point. The onset flow is used to determine the relative onset flow (U_{rel}) and inflow angle (ϕ) to the blade at each position along the blade, as shown by Eqs. (8)–(9).

$$\delta U_{rel}(t) = \sqrt{U_X^2 + (\Omega r - U_\phi)^2} \quad (8)$$

$$\delta \phi(t) = \sin^{-1} \frac{U_X(t)}{U_{rel}(t)} \quad (9)$$

Where U_{rel} is the relative velocity to the blade which incorporates the longitudinal velocity, defined by $U_X = U_0(1 - a)$ with a being the mean axial induction factor and the components in the tangential direction, U_ϕ with the angular velocity ω and each radius r . The lift and drag force on each blade segment vary according to Eqs. (10)–(11).

$$\delta L(t) = \frac{1}{2} B \rho c (U_{rel})^2 C_L \delta r \quad (10)$$

$$\delta D(t) = \frac{1}{2} B \rho c (U_{rel})^2 C_D \delta r \quad (11)$$

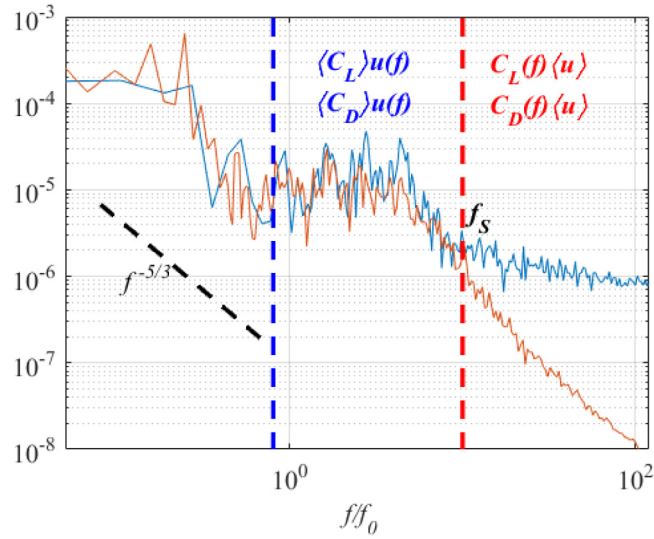


Fig. 4. Example of the spectra of lift coefficient at a specific angle of attack (blue) with fluctuating component of the onset relative velocity (orange). This spectra is divided into low, mid and high frequency ranges, with the key areas of influence for the magnitude of the unsteady lift and drag. In the mid range only a mean lift and drag are considered. In the high frequency range the magnitude of the fluctuating part is used in conjunction with the mean velocity and aggregated onto the original load spectra. (For interpretation of the references to colour in this figure legend, the reader is referred to the web version of this article.)

Where c is the chord length, δr is the radial width of the blade segment, B is the number of blades, ρ is the fluid density, C_L and C_D correspond to the lift and drag coefficients respectively. Using the calculated lift and drag forces for each blade the axial (F_a) and tangential (F_t) forces along each blade are calculated using Eqs. (12)–(13).

$$\delta F_a(t) = \delta L(t)\cos(\phi(t)) + \delta D(t)\sin(\phi(t)) \quad (12)$$

$$\delta F_t(t) = \delta L(t)\sin(\phi(t)) - \delta D(t)\cos(\phi(t)) \quad (13)$$

The main interest here is the axial force (F_a) on each segment of the blade as this leads to the calculation of root bending moment as well as rotor thrust. These results can be used to establish the respective load spectra and hence determine the load cycles enabling the fatigue loads to be predicted for the blades and rotor.

3.3. Extension of the load spectra

The method used to determine the loading experienced by each blade is outlined in the previous Section. However, this method assumes all loads on the blade section are quasi-steady and therefore neglects loads at higher frequencies. A 2D CFD model is employed to determine load fluctuations caused by unsteady flow around the blade and blade generated turbulence. To illustrate this an example of the lift coefficient spectrum, and the corresponding relative velocity spectrum is shown in Fig. 4.

The spectra has been divided into three adjacent frequency bands, to highlight the dominant fluctuating components. For the low and high frequency range the fluctuating component of velocity follows the energy decay trend of $-5/3$, which is expected. In the mid-frequency range (highlighted by the blue line), the magnitude of the lift and velocity are very similar, only in the high frequency range (highlighted by the red line) is there any variation between the two magnitudes. This variation shows that there is an increase in the magnitude due to the lift coefficient, hence the force coefficients are considered to dominate in this range and can be combined with the mean velocity to determine additional loading. Unsteady lift and drag coefficients are calculated, and incorporated in the blade load model as follows:

1. Using the onset flow velocity, calculate the mean angles of attack across the blade, at each radial position (α_i).
2. Generate spectra of lift and drag coefficients using the time-varying onset relative velocity obtained for different radial positions, using the mean angles of attack.
3. Determine the separation frequency (f_s) at which the C_L/C_D fluctuations dominate the unsteadiness, using the gradients in the high frequency section for the onset flow and lift coefficient, as shown in Fig. 4 for the lift coefficient.
4. Calculate the energy in the spectra above the calculated separation frequency, across a range of frequency bins for each angle of attack.
5. Calculate the magnitude of the lift and drag coefficients ($C_L(f)$ and $C_D(f)$) for each angle of attack (α_i) at each frequency bin.

The magnitude of the lift and drag fluctuations are incorporated into the BEM theory, by modification of Eqs. (10)–(13) to determine the axial force per segment of the blade at each binned frequency, defined by 'j'. This is used in the frequency domain through a Discrete Fourier Transform (DFT) in order to determine the magnitude of the resultant spectra, given by Eq. (14).

$$F_n = \sum_{j=0}^{N-1} dL_i(f_j) e^{-2\pi i n j / N} \quad (14)$$

Where $dL_i(f_j)$ is the lift force varying with frequency bin, the fluctuating lift coefficient is applied to calculation of lift force through Eq. (15), which is applied in the same way for the drag coefficient.

$$dL_i(f_j) = \frac{1}{2} \rho c_i \langle U_{rel,i} \rangle^2 |C_L(f_j)_i| dr_i \quad (15)$$

These force spectra, comprising both a component that is dependent on a mean lift coefficient for frequencies less than f_s and an unsteady lift coefficient for higher frequencies, combine to give Eq. (16).

$$dFa_i(f_j) = dL \cos(\langle \phi_i \rangle) + dD \sin(\langle \phi_i \rangle) \quad (16)$$

3.4. Quantifying the design life

The design life can be quantified using Damage Equivalent Loads (DEL). These loads are defined as the fatigue damage caused by a single load value repeating at a single frequency, as shown in Eq. (17). This method has been used by Freebury and Musial (2000) for wind turbine calculations where the specific materials are not known. These loads do not specify the value of load that a component can withstand during its lifetime, but rather quantifies the load it experiences undergoing certain unsteady conditions.

$$L_m = \left(\frac{\sum_i n_i L_i^m}{fT} \right)^{\frac{1}{m}} \quad (17)$$

Where L_i is the load at bin i , m is a material property given by the slope of the S–N curve for the material, T is the length of time for the turbine operation, f is the repetition frequency and n_i is the number of cycles at a given load, determined by a cycle counting method. A common method for counting cycles of a varying magnitude is Rainflow cycle counting. This method was originally defined by Endo et al. (1974) and has been used to calculate loading on offshore components (McCann et al., 2007; Weller et al., 2015; Parkinson and Collier, 2016). When blade loading is considered, the material property is defined by a semi-flexible composite, in this study a material gradient of $m = 10$ is used. To determine the lifetime of the component, more specific material knowledge would need to be used in addition to the calculation of the damage fraction based upon the number of load cycles. This is not considered further in the present study.

4. Unsteady 2D lift and drag

4.1. Model set up

Conventional BEMT methods utilise tables of lift and drag coefficients for specific aerofoils at Reynolds numbers around the steady-state condition. These lift and drag forces do not vary with the change in unsteady onset flow conditions. One method for utilising the change in lift and drag forces over time is to analyse the power spectra produced, from varying onset conditions. The time varying onset flow to the blade is determined relative to the blade using one position along the radius (0.7R). A 2D CFD model is created using the commercial software ANSYS-FLUENT, for the aerofoil blade segment, which corresponds to a NACA 63-818 profile. This profile is used as it represents the same section on the experimental turbine used in Payne et al. (2018) and is shown in Fig. 5. A two dimensional profile is used here as it sufficiently captures the lift and drag variation without the computational expense of a three dimensional model, when modelling at a Reynolds number around 10^5 , Martinat et al. (2008).

The aerofoil is studied using a C-shape mesh created using CFD-ICEM, allowing for varying inflows, a RANS solver is used and considered suitable for analysis of a 2D aerofoils for tidal turbines, based upon previous work (McNaughton et al., 2012, 2014) and Sequeira and Miller (2014). Three mesh cases were initially examined with differing refinement, but all with a higher level of refinement surrounding the aerofoil, the size of the total domain is greater than shown in Fig. 5, with it spanning a radius 12 times the chordlength of the aerofoil. Within the RANS model the $k-\omega$ SST model is used, Menter (1994), with grid convergence examined using Richardson extrapolation. Initially, a Reynolds (Re) number of 800k was studied for validation with experimental data from Guo et al. (2015). From this comparison the lift and drag results obtained were in better agreement with the experimental data than values obtained using XFOil. Simulations were then performed at a lower Re number (181k) representative of the value, local to the blade segment, from the experiments in Payne et al. (2018).

Fig. 6 shows a comparison between the lift and drag ratio at each Re number. Better agreement is found using the steady CFD simulations than the XFOil values. In each simulation conducted for the mesh convergence study there is a higher level of refinement surrounding the aerofoil and a scale ratio between cells no greater than 1.2. With a target Y^+ value greater than 30 and a cell spacing, $\Delta s > 0.0035c$, where c is the chordlength.

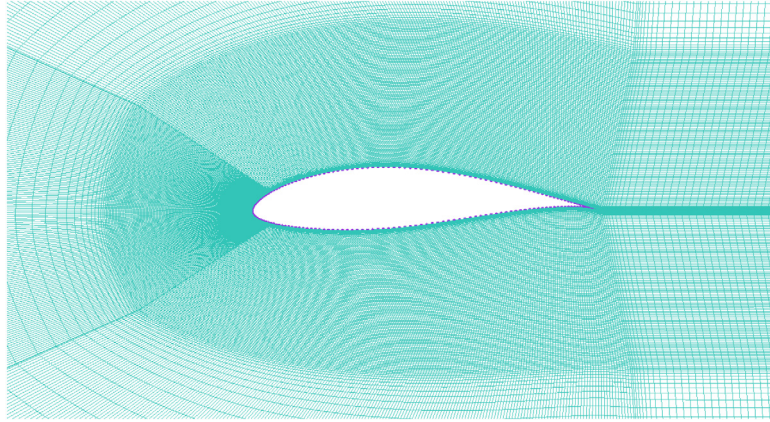


Fig. 5. Aerofoil at the 0.7R blade segment, with surrounding mesh, showing areas of refinement closest to the aerofoil.

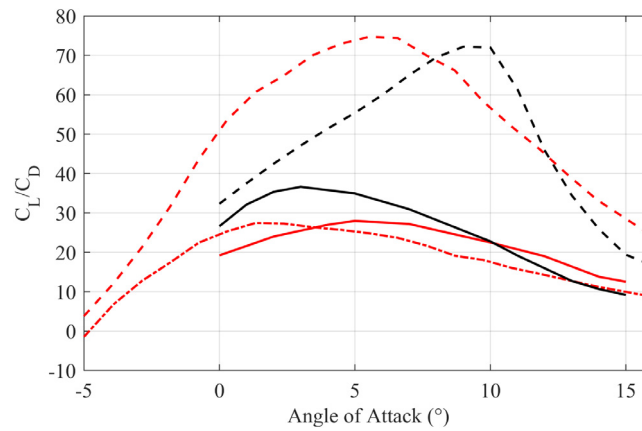


Fig. 6. Ratio of lift and drag coefficients with angle of attack for XFOIL results for $Re = 800,000$ (red dash), experimental results for $Re = 800,000$ (red dashdot) Guo et al. (2015), CFD results for $Re = 800,000$ (red solid), XFOIL results for $Re = 181,000$ (black dash) and CFD results for $Re = 181,000$ (black solid). (For interpretation of the references to colour in this figure legend, the reader is referred to the web version of this article.)

4.2. Unsteady force coefficients

The resultant unsteady lift and drag forces are determined for a range of angles of attack using the relative onset velocity from the two turbulence methods over a time representing 25 rotations of the turbine. Fig. 7 is included to show the steady lift and drag coefficients determined using a mean relative onset flow, comparable to the ratio shown in Fig. 6, along with the variation due to the unsteady onset flow at constant angles of attack. The variation in lift and drag coefficient increases when the SEM is used for the inflow instead of the von Kármán method. Across the inflow angles of interest, the change in lift and drag coefficient caused by the varying onset flow is greater than for a change in ambient turbulence intensity, Harvey et al. (2021).

This study focuses on using the magnitude of the variation of lift and drag coefficients which arise from an unsteady inflow to the blade. Both turbulence generation methods show this variation across the inflow angles of interest. The spectra of the CFD predictions of time-varying lift and drag are compared to the spectra of onset relative velocity fluctuations. An example has been shown in Fig. 4. A key point here is to identify the frequency at which the coefficient of lift force spectra diverges from the velocity spectra has been found to be dependent on the inflow angle to the blade. An initial study into the variation of frequency separation with angle of attack is shown in Fig. 8 with examples given for both turbulence generation methods.

The range of angles used to calculate the separation frequency includes all the angles the chosen radial position on the blade experiences, with all occurring before stall. This does not account for any changes in dynamic stall caused by the varying inflow conditions which has been considered in Scarlett (2019), which may increase the stall angle. The variation is described by Eq. (18) for the von Kármán turbulence method and Eq. (19) for the SEM turbulence.

$$f_{S,VK} = 57.7f_0\alpha^{-0.7} \quad (18)$$

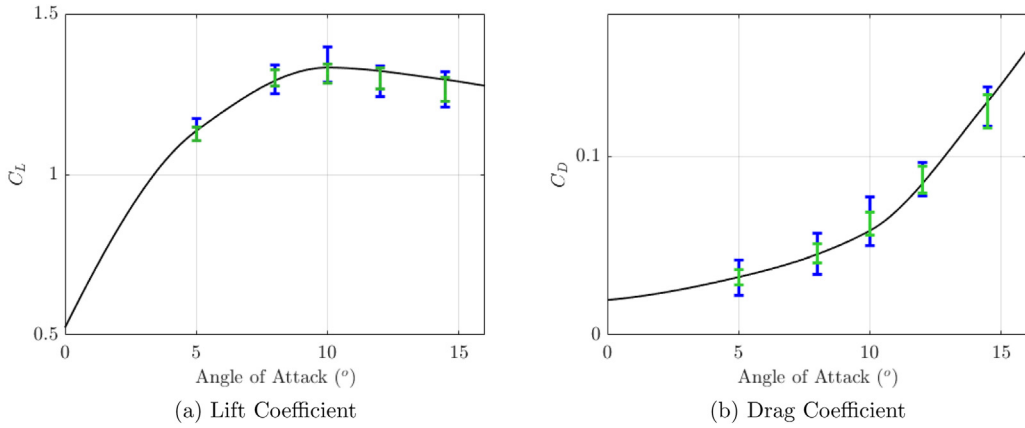


Fig. 7. Inter-quartile range of lift and drag coefficients for the von Kármán method (green) and the SEM (blue), refer to online version for colour. (For interpretation of the references to colour in this figure legend, the reader is referred to the web version of this article.)

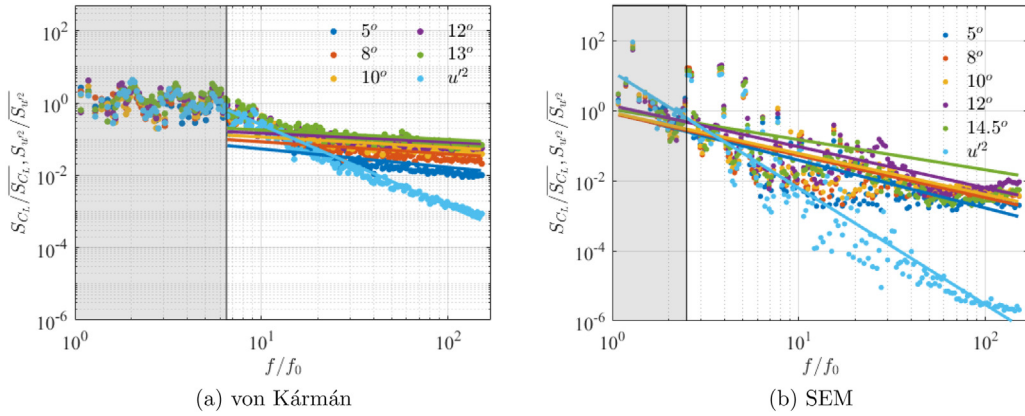


Fig. 8. Examples of normalised lift coefficient and onset velocity spectra for both turbulence methods, to show the gradients in the high frequency range and the separation point for each given angle of attack. (For interpretation of the references to colour in this figure legend, the reader is referred to the web version of this article.)

$$f_{S,SEM} = 7.3f_0\alpha^{-0.45} \quad (19)$$

Where $f_{S,VK}$ is the separation frequency of for von Kármán method, and $f_{S,SEM}$ is for the SEM, f_0 is the rotational frequency and α is the angle of attack.

These frequency separation points are determined from the separation of lift coefficient only. This is due to the lift coefficient having more impact on the load fluctuations, therefore, the magnitude of the drag coefficient is calculated after using the same frequency separation equations.

4.3. Influence of operating point

By including the magnitude of the fluctuating component of the lift and drag, the high frequency tail of the spectra is altered. The separation frequency depends on the turbulence method, with the operating point having no affect. However, the magnitude of the fluctuating component is found to vary with the operating point. Only using the variation of the resultant lift and drag from the relative velocity at a TSR of 5.89, does not allow for a change in the variance due to different relative velocities and angles of attack caused by alternative onset flow cases. The influence of the rotational speed on the magnitude of the fluctuations is investigated using the same CFD model with modified inflow to account for a change in relative velocity. The gradient across the mid to high frequency range is defined by the relationship shown in Eq. (20).

$$G_S = f^m e^p \quad (20)$$

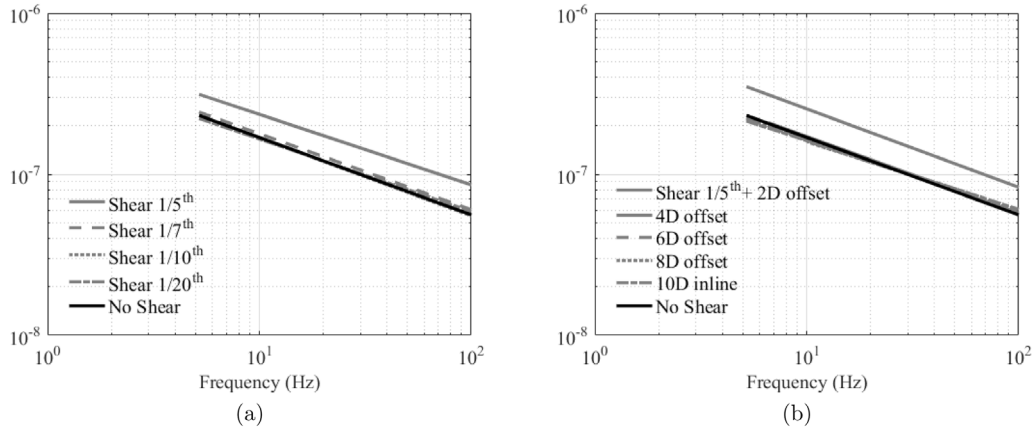


Fig. 9. Variation in trend of the high frequency lift coefficient with (a) vertical shear profiles applied and (b) both transverse and vertical shear profiles applied.

Where G_S is the gradient of the tail end of the spectra, which varies with frequency, f . The constants for the magnitude and gradient of the high frequency tail for differing TSRs and angles of attack on the lift and drag spectra, are determined using Eqs. (21)–(24) for the von Kármán method and Eqs. (25)–(28) for the SEM.

$$m_L = (-0.031(\log(\alpha)) + 0.766)\log(\lambda) - 1.55 \quad (21)$$

$$p_L = (1.53(\log(\alpha) - 6))\log(\lambda) - 8.5 \quad (22)$$

$$m_D = (-0.004\alpha - 0.04)\lambda + 0.05 \quad (23)$$

$$p_D = (0.04\alpha + 0.31)\lambda - 17.7 \quad (24)$$

$$m_L = (0.2(\log(\alpha)) + 0.05)\log(\lambda) - 1.8 \quad (25)$$

$$p_L = (2(\log(\alpha)) - 8.5)\log(\lambda) - 2.5 \quad (26)$$

$$m_D = (-0.008\alpha + 0.223)\lambda - 1.5 \quad (27)$$

$$p_D = (-0.0192\alpha - 0.35)\lambda - 13 \quad (28)$$

Where subscript D is for drag and L is for lift and λ is the TSR value. These relationships are used to determine the magnitude of the lift and drag contribution from blade scale fluctuations on the blade loads with operating point, for comparison to experimental results in Section 5.

4.4. Influence of unsteady conditions

In addition to the turbine rotating at different speeds, the inflow to the blade will also vary due to the application of different unsteady onset conditions. The conditions applied here mainly influence the signal component of the periodic loading, as seen in Fig. 3, however, variations in the noise can be caused by the turbulence characteristics and the method of generation. To determine the influence of these shear profiles, additional simulations have been conducted, which correspond to both vertical and transverse shear being experienced by the turbine, all at a constant angle of attack. The results from a selection of these simulations are shown in Fig. 9. The vertical shear profile applied with increasing indices results in little change to the magnitude of the high frequency fluctuations until a shear of $1/5^{\text{th}}$ is applied. This shear profile leads to an increase of 2.4%. The gradient of the resulting high frequency trend varies by less than 7% across the different profiles, however, this variation is considered to have less effect when imposed on the high frequency loading than a change in magnitude. Examining the variation in magnitude due to the transverse shear results in a 3% increase in magnitude for the wake offset greater than 6D. Fig. 9(b) shows the increase for a transverse case with the largest shear index and wake deficit, as well as a range of other offset cases.

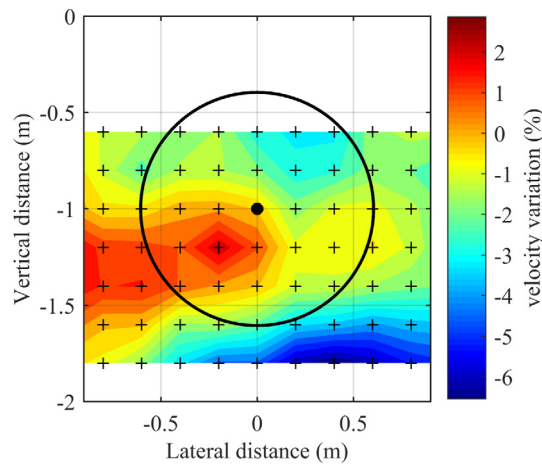


Fig. 10. Velocity variation across the rotor plane, obtained from the IFREMER test facility in Boulogne-Sur-Mer, [Payne et al. \(2018\)](#). (For interpretation of the references to colour in this figure legend, the reader is referred to the web version of this article.)

5. Comparison to experiment

Initially, the blade loading results are compared to the experiments performed in the X-MED project. This comparison establishes the difference in loading between running an efficient BEM method using synthesised turbulence to the experimental results. To perform this comparison the properties of the onset flow are used. This includes turbulence parameters as specified in Section 3.1, as well as an appropriate shear profile. The shear profile determined within the IFREMER test flume is not as significant as a strict 1/7th power law profile, therefore, for this comparison, the shear profile is taken from the average velocity variation across the rotor plane, as shown in Fig. 10, from [Payne et al. \(2018\)](#).

The load spectra for the root bending moment is shown in Fig. 11. This spectra is calculated using the method described in Section 3.2 without the high frequency fluctuations for the original case. This comparison is made by considering different operational conditions which contribute to the unsteady loading at one 'quasi-steady' moment in time. These conditions include accounting for the effect of tower shadow through the use of potential flow theory, following the method which is applied for wind turbines in [Bianchi et al. \(2006\)](#), as well as the shear of the onset flow. The original root bending moment spectra, shown in Fig. 11, for both methods gives a consistent decay across the high frequency range of the spectra. This is not found in the experimental load spectra. To better represent the high frequency range the loading due to the magnitude of the lift and drag fluctuations is included and increases the gradient of the high frequency range. For the von Kármán case the increase in the spectra is smaller than for the SEM case. One of the contributing factors to this difference is the separation frequency (f_s) which has a smaller value for the SEM case and therefore a larger band of frequencies are influenced by the lift and drag fluctuations. The increase in magnitude, for both turbulence methods, decreases the gradient of the root bending moment spectrum in the high frequency range, with both magnitude and gradient in good agreement with the experimental measurements. The improvement is particularly notable for the onset flow defined by SEM for which only low frequency, large amplitude velocity fluctuations are generated in the onset flow.

The total load cycles, and the damage equivalent loads, are calculated from the time varying root bending moment for each case. Load cycles are calculated using the Rainflow counting method, with each cycle placed within a pre-described load bin. The number of cycles within each load bin, are shown through the cumulative number of cycles in Fig. 12. These cyclic load amplitudes allow for the calculation of DELs, as shown in Eq. (17). Herein the repetition frequency used is chosen as the rotational frequency of the turbine (f_0), to facilitate comparison between the reported DELs.

The increase in the gradient over the mid to high frequency range has little impact on the large amplitude cycles, but it has more impact on the smaller amplitude load cycles. These smaller amplitude load cycles increase by a small amount for the von Kármán turbulence, and by a much greater amount for the SEM. This increase in load cycles is expected due to the increase in high frequency fluctuations, which are lacking when the frozen turbulence field is set up using this method.

The resultant DELs from the root bending moment for the different methods are shown in Fig. 13. Without the addition of the high frequency fluctuations the damage equivalent loads for the von Kármán method are 19% lower than the experimental value and 15% higher for the SEM case. However, the additional load cycles caused by the high frequency fluctuations result in an increased DEL for the von Kármán case, to within 7% of the experimental value, and a decrease for the SEM case, to within 2% of the experimental value. These comparisons to the experiment are for a single TSR value. Results for a wider range of operating points are shown in the next Section.

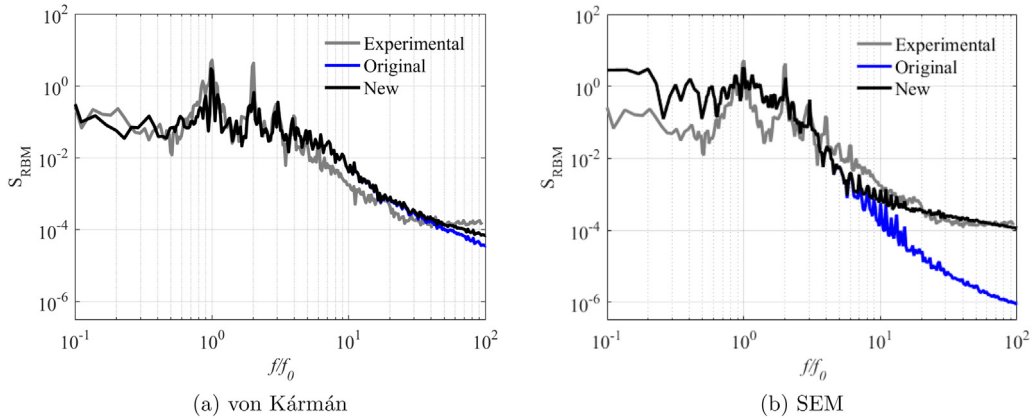


Fig. 11. Load spectra for the root bending moment for each turbulence method, where the original spectra (blue) is calculated using steady lift and drag coefficients within calculation for axial force on the blade, the 'new' (black) spectra includes the magnitude of the lift and drag fluctuations in the axial force calculation. (For interpretation of the references to colour in this figure legend, the reader is referred to the web version of this article.)

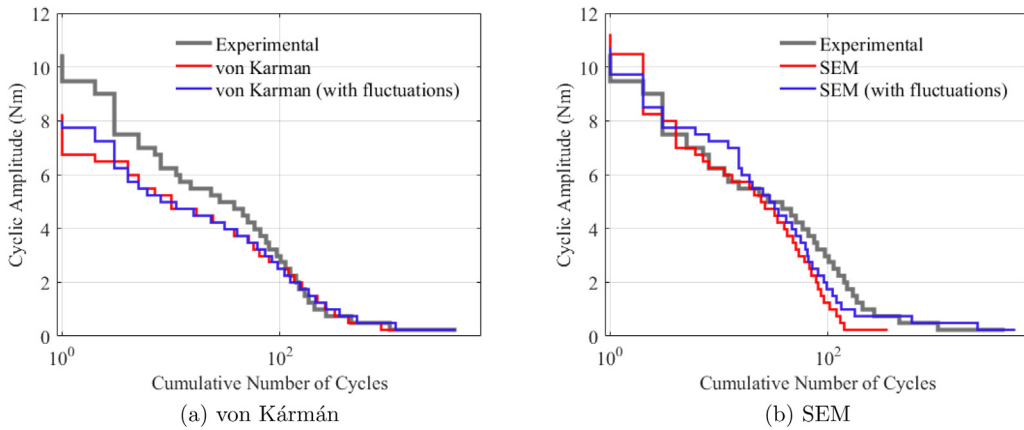


Fig. 12. Cumulative load cycles determined from blade loading, for the experimental case (black), each turbulence generation method (red) and each method with the magnitude of the high frequency load fluctuations included (blue). (For interpretation of the references to colour in this figure legend, the reader is referred to the web version of this article.)

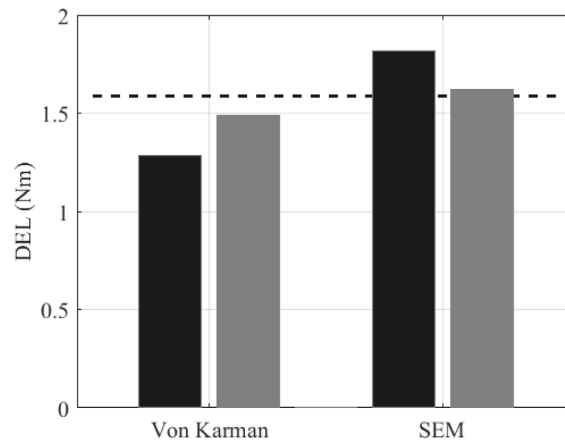


Fig. 13. Damage equivalent loads calculated from the root bending moment, experimental value (dashed line), and for the two turbulence generation methods, loads from original spectra (black), loads with high frequency fluctuations included (grey).

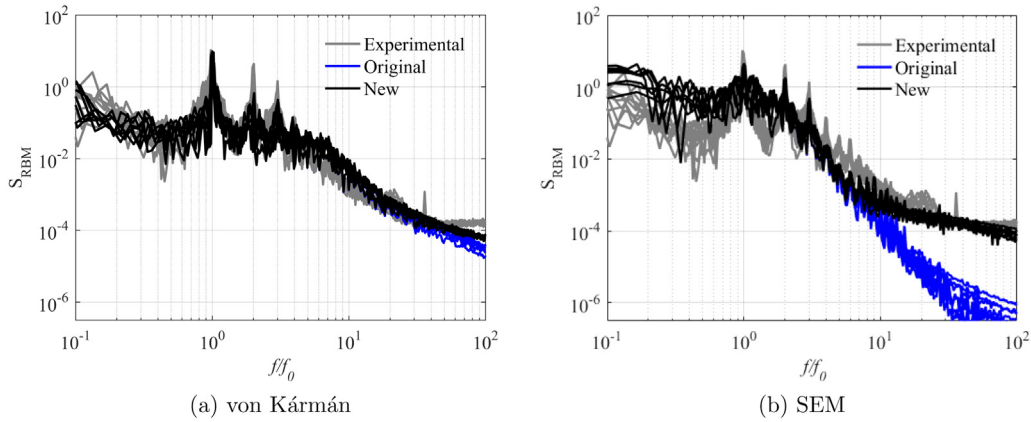


Fig. 14. Load spectra for the root bending moment for each turbulence method for a range of operating points, experimental spectra (grey), original spectra (blue) and the new spectra including the high frequency fluctuations (black). (For interpretation of the references to colour in this figure legend, the reader is referred to the web version of this article.)

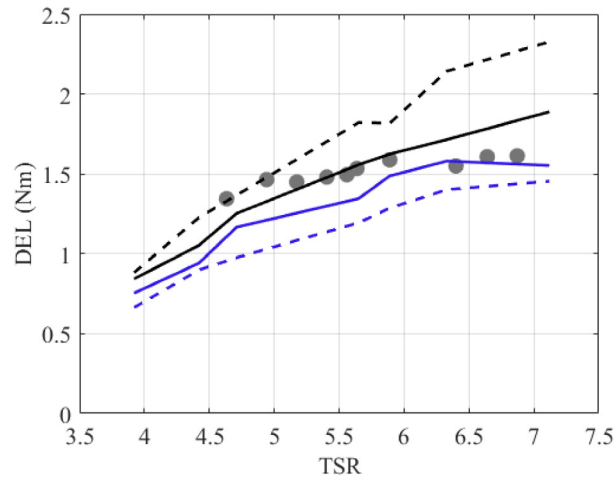


Fig. 15. Damage equivalent load magnitude for the two turbulence generation methods, (black) for the SEM and (blue) for the von Kármán method, with (solid) and without (dashed) the inclusion of the magnitude of the fluctuating load, compared to the experimental value (grey markers). (For interpretation of the references to colour in this figure legend, the reader is referred to the web version of this article.)

5.1. Variation in operating point

During the experiments in [Payne et al. \(2018\)](#), multiple TSRs were used to determine the loads on the device. Using the variation in gradient of the high frequency range shown by Eq. (20) in Section 4.3, a range of different operating points have been used to determine the blade loads. Fig. 14 shows the load spectra for the root bending moment for one blade at each TSR value for each turbulence generation method compared to the experimental spectra. Where the original spectra is calculated using steady lift and drag coefficients for axial force on the blade, the new spectra includes the magnitude of the lift and drag fluctuations in the axial force calculation for the different gradients applied for each TSR. The inclusion of the lift and drag fluctuations over the high frequency range, result in a convergence between the different operating points and a similar magnitude to the experimental spectra.

Following the same process as for the single TSR case, the load cycles are calculated for each TSR case using the time history of root bending moment from the new load spectra. These load cycles are used to calculate the range of DELs as shown in Fig. 15. Across the range of TSR, the influence of the inclusion of the high frequency fluctuations is consistent with the single TSR results, with the DELs for the SEM case reducing with the increase in load cycles and the DELs increasing for the von Kármán case. In comparison with the experimental results, the overall trend shown for both of the two turbulence generation method is an increase of DEL with TSR, which is not replicated with the same gradient for the experimental case.

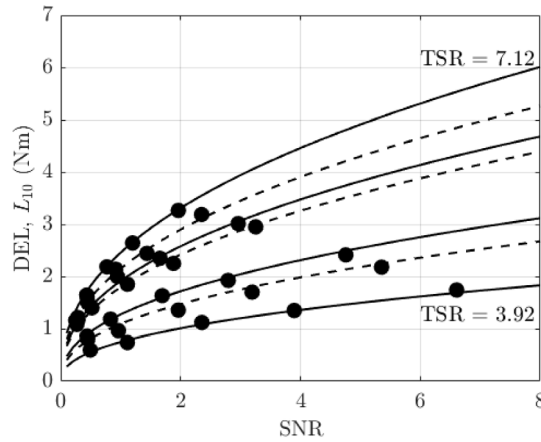


Fig. 16. Variation of DEL with SNR value for the von Kármán method with increasing TSR, with the solid lines showing the cases used to calculate DEL/SNR relationship, and the dashed lines for the remaining TSR cases, with the solid markers representing calculated SNR values for the range of DEL.

6. Application to unsteady conditions

The onset flow used in the experimental comparison presented in the preceding section is defined by the conditions measured in the test facility. The flow is not strictly a vertical shear profile typical of a channel flow but comprises a mixture of vertical and transverse shear. This section examines variation of fatigue load, characterised by DEL, over a range of onset flows. Steady flows are defined as in Section 3.1, turbulence generated with the von Kármán method and each flow is characterised by the SNR. This analysis aims to establish whether the signal to noise definition of unsteady conditions contribute to the DELs, to discover the level of understanding required to determine the fatigue loads. In Section 3.1 the relative onset flow to the blade is defined, with the spectra shown in Fig. 2. This spectra is shown for one TSR value with no additional onset flow conditions, it is only determined from the turbulent flow field. Subsequently, additional onset flow conditions are described, with the fatigue loads from these conditions calculated.

Firstly, SNR values are determined for a range of TSR values for a variety of onset flow conditions. Initially, four TSR values are used to determine the relationship between the DELs and the SNR values with TSR, this relationship is given by Eqs. (29)–(30). The SNR values are calculated by filtering the original fluctuating onset flow (U_{rel}) at 0.7R to determine the variance of the noise component, in this case a low pass 6th order Butterworth filter is used with a cut off frequency of $10f_0$.

$$X = 2.86 \ln(\lambda) - 3.16 \quad (29)$$

$$R = X(SNR)^{0.43} \quad (30)$$

Where X determines the magnitude of the relationship which varies with TSR (λ) and R describes the relationship between the damage equivalent load and the SNR value. As a result of these equations the relationship between DEL and SNR for the range of TSR values is shown in Fig. 16.

Those which use the actual TSR results are shown by solid lines, and the three estimated trends are shown by the dashed lines with the calculated DEL and SNR for these TSR values. This shows that the overall trend calculated from a smaller set of TSR values can adequately predict the DELs for additional TSRs based upon their SNR values. The trends determined for the von Kármán method have been calculated using the range of SNR values determined from a series of vertical shear profiles. This range of SNR values describe the DEL for five different cases of vertical shear, with the lowest corresponding to no additional vertical shear and the highest SNR value found for a 1/5th power law. As the power law index increases the periodic loading increases and causes a larger magnitude signal and higher SNR value. For the lower TSR values a greater magnitude signal is found than for the higher TSR cases, which results in larger SNR values as overall magnitude of the noise for the von Kármán turbulence field stays constant.

In addition to using the vertical shear profiles to provide varying onset flow, a series of conditions can cause onset flow variations, such as the transverse wakes explained in Section 3.1. These additional conditions are examined for one TSR value (5.89) and are used to compare to the trends based on Eqs. (29)–(30), and is shown in Fig. 17.

The series of red markers shown in Fig. 17 correspond to additional transverse shear cases and their combinations with the four different vertical shear profiles. For each case the peak signal value is determined through examining the magnitude at the rotational frequency and subsequent harmonics. With the variation in onset shear and wakes, the peak signal for some offset wake cases will occur at the second harmonic, as seen in Fig. 3(c). By including the additional shear

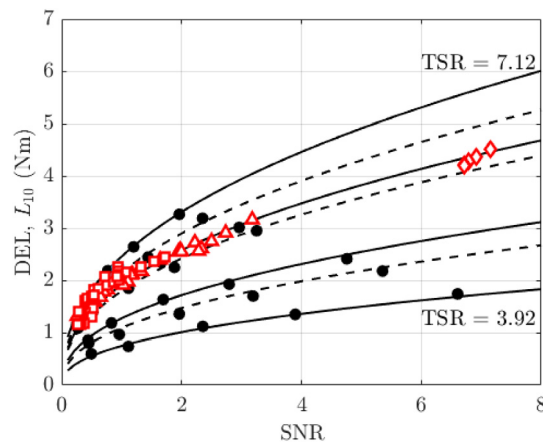


Fig. 17. Variation of DEL with SNR value for the von Kármán method with increasing TSR, red markers for additional vertical and transverse shear combinations at a TSR of 5.89. (For interpretation of the references to colour in this figure legend, the reader is referred to the web version of this article.)

profiles the SNR to DEL relationship continues to follow the trend determined from the vertical only shear cases. The collection of DEL values with an SNR value less than 1 represent those cases where the peak is caused by a weak shear profile, where the signal is of less magnitude than the variance of the noise. These points include the cases where the turbine is experiencing the maximum velocity deficit from a wake 2D downstream, inline with an upstream turbine. When determining the peak signal for these, unlike the other cases shown, the large velocity deficit variation across the rotor results in a dominant second harmonic. Although this is accounted for when determining the SNR value, it does reduce the peak magnitude when compared to using the peak magnitude from the first harmonic. When the SNR value increases and is greater than 1, there are a series of cases which are well represented by the predicted trend. The collection of cases at $\text{SNR} > 6$ correspond to the maximum velocity deficit across the entire rotor area, representing a turbine located 2D downstream, offset to an upstream rotor, with the wake deficit combining with the series of vertical shear profiles to give a slight change in signal magnitude. For each velocity deficit caused by transverse wakes the additional vertical shear increases the damage equivalent load corresponding to the magnitude of the shear index. In reality, the variation in velocity deficit experienced from a turbine located very closely downstream is not a common onset flow experienced by the turbine, in addition, the profiles used here to demonstrate a variety of downstream wake positions have been shown to capture profiles greater than 6–8 diameters, [Lande-Sudall et al. \(2018\)](#).

7. Discussion

This study looks to improve the understanding of the influence of unsteady loading at the blade scale and its influence on turbine blade design. It has been shown that consideration of the blade load spectrum as the sum of a quasi-steady load, due to a mean lift coefficient, and higher frequency load due to an unsteady lift coefficient, improves prediction of the load spectrum and fatigue load relative to quasi-steady BEMT only. This is shown for turbulent onset flows generated using both a von Kármán spectral method and a Synthetic Eddy Method. Load predictions are based on the variation of lift and drag generated from a 2D aerofoil for a blade section. Although simplified this approach is considered representative and is consistent with the use of steady lift and drag data in standard BEMT models. 3D analysis of aerofoil loading may provide greater insight to the flow physics local to the blade. However, if extending to 3D it would be preferable to consider the impact of the along blade flow (radially in the context of a turbine blade). Studies have shown the impact of this flow three-dimensionality on rotation of the lift vector near tip (e.g. [Wimshurst and Willden \(2018\)](#)) but the effect on unsteady loads remains to be explored further. The main parameters derived from the 2D blade analysis are the separation frequency and the magnitude and slope of the lift spectrum at higher frequencies. Here these are characterised by rotor TSR and mean angle of attack. This has only been characterised for one blade geometry, of a laboratory scale turbine. The mean angle of attack is below stall angle for all cases so similarities are expected to other foil geometries prior to flow separation. However, further analysis would be required to establish these parameters for alternative aerofoil sections. This would be for a similar range of angles of attack and of turbulence intensity of the relative velocity, which are expected to be representative due to dependence on typical values of TSR and radial position. Despite the relative simplicity of a 2D sectional analysis the method to determine the blade loading on the turbine provides good agreement with the experimental results from a lab scale turbine. With all the modelling performed on a lab scale blade and appropriate Reynolds number, application to a full scale system would require scaling.

Different onset flows, regardless of the combination of shear, wake and turbulence that define the onset flow can be characterised in terms of SNR. By defining onset flows in terms of SNR a relationship is identified with damage equivalent

load increasing with SNR, of the flow, and with tip speed ratio, of the turbine. This approach is also applied to more complex onset flows, including profiles representative of upstream turbine wakes, with comparable relationships between SNR and DEL despite the more complex onset flows. Applicability to more complex onset flows, such as in-array onset flows, or turbulent flows co-existing with waves, remains to be assessed. The analysis to determine DEL variation with SNR has been conducted solely for the von Kármán turbulence generation method. Further work on examining the use of the SNR to characterise the relative onset flow to determine the change in DEL for turbine blades would include using additional turbulence generation methods. This would involve investigating using both an isotropic and anisotropic set up of the Synthetic Eddy Method with a greater variation in the eddy sizes distributed through the turbulent flow field, similar to the work conducted in [Togneri et al. \(2020\)](#), which would remove the potential need for additional filtering on the SEM case to determine the signal peaks. This method uses the relative velocity determined and used in the CFD simulations, and therefore does not account for the additional turbulent noise found in the von Kármán method when compared to the Synthetic Eddy Method.

8. Conclusions

The unsteady loading on the blade of a laboratory scale 3 blade tidal turbine is modelled using blade element theory with an inflow developed using frozen turbulence models. Based upon this the damage equivalent loads are determined to within 15% of the loading on an experimental 1.2 m diameter turbine. Inclusion of high frequency variation of lift and drag in the blade element model improves prediction accuracy. Damage equivalent loads are obtained to within 7% when using the von Kármán method to generate turbulence and to within 2% of the experimental value when using the SEM inflow. The improvement in the DEL prediction is obtained by a better prediction of the mid to high frequency load fluctuations experienced on the blade and the corresponding load cycles. The high frequency load fluctuations have been defined by the gradient of both lift and drag spectra, obtained from 2D CFD with relative velocity defined for each turbulence generation method and for a range of mean angles of attack. For a range of operating points of the turbine the definition of the gradient has resulted in a similar magnitude in the load spectra across the mid to high frequency for both turbulence generation methods. When comparing the DEL across the range of TSR from the experiment the inclusion of the high frequency fluctuations has resulted in closer results from both turbulence generation methods, which follow the same trend of increasing DEL with TSR. However, the gradient with TSR is greater for the predictions than the experimental values.

This analysis uses a 2D aerofoil to assess the load fluctuations from blade scale flow. Whilst high order 3D CFD may be required for full prediction of loads during flow separation and due to dynamic effects, for the conditions studied here the flow remains largely attached and 2D RANS CFD is employed, with inflow conditions to the blade defined by the onset turbulence method. For the von Kármán onset turbulence, predictions are only slightly changed as the separation frequency between the onset turbulence fluctuations and the lift and drag is higher than for the case with the synthetic eddy method. With the SEM inflow the separation frequency is much lower due to the coherency and lack of high frequency turbulence fluctuations, so the influence of the blade scale flow on the load cycles has a much greater effect.

Characterisation of the onset flow to the blade in terms of the signal to noise ratio, enables the magnitude of the stochastic and deterministic components of the flow field to be captured. This ratio is determined for the von Kármán turbulence generation method, and shows the variation of DEL with SNR, where the increase in DEL with increasing SNR is found. This is expected as the background noise level for the turbulence generation method is set as the intensity level and remains fairly constant, and the increase in deterministic shear results in both a higher signal value and an increase in larger load cycles. When a number of different onset flow conditions are used, the relationship between the SNR and DEL can be well determined, with an increase by a factor of 3.3 on the DEL for one SNR value. When one value of TSR is considered, for the largest range of SNR, the DELs can vary by a factor of 6.5.

This work provides confidence in the prediction of unsteady loads using alternative turbulence generation methods, with similar fatigue loads predicted when unsteady lift is modelled using two turbulence models. The characterisation of various onset flows by SNR of relative velocity allows for identification of relationships between onset flows due to differing shear, wakes and turbulence, and the resultant damage equivalent loads. Evaluation of this approach for more complex flows such as the wakes occurring in turbine arrays, and due to interaction of turbulence with surface waves, remains to be evaluated.

CRediT authorship contribution statement

H. Mullings: Conceptualization, Methodology, Software, Validation, Analysis, Writing – original draft. **T. Stallard:** Conceptualization, Writing – review & editing, Supervision, Funding acquisition.

Declaration of competing interest

The authors declare that they have no known competing financial interests or personal relationships that could have appeared to influence the work reported in this paper.

Acknowledgements

The research conducted was supported by an EPSRC DTP studentship (EP/P117127), a President's Doctoral Scholarship from The University of Manchester and the Supergen ORE hub (EP/S000747/1).

References

- Afgan, I., McNaughton, J., Rolfo, S., Apsley, D., Stallard, T., Stansby, P., 2013. Turbulent flow and loading on a tidal stream turbine by LES and RANS. *Int. J. Heat Fluid Flow* 43, 96–108. <http://dx.doi.org/10.1016/j.ijheatfluidflow.2013.03.010>, URL <http://linkinghub.elsevier.com/retrieve/pii/S0142727X13000672>.
- Ahmed, U., Apsley, D., Afghan, I., Stallard, T., P.K., S., 2017. Fluctuating loads on a tidal turbine due to velocity shear and turbulence: Comparison of CFD with field data. *Renew. Energy* 235–246. <http://dx.doi.org/10.1016/j.renene.2017.05.048>, arXiv:arXiv:1011.1669v3.
- Apsley, D.D., Stallard, T., Stansby, P.K., 2018. Actuator-line CFD modelling of tidal-stream turbines in arrays. *J. Ocean Eng. Mar. Energy* <http://dx.doi.org/10.1007/s40722-018-0120-3>, URL <http://link.springer.com/10.1007/s40722-018-0120-3>.
- Apsley, D.D., Stansby, P.K., 2020. Unsteady thrust on an oscillating wind turbine: Comparison of blade-element momentum theory with actuator-line CFD. *J. Fluids Struct.* 98, 103141. <http://dx.doi.org/10.1016/j.jfluidstructs.2020.103141>.
- Atlantis, S., 2018. The meyen project. URL <https://simecatlantis.com/projects/meyen/>.
- Bianchi, F.D., De Battista, H., Mantz, R.J., 2006. *Wind Turbine Control Systems*, vol. 26. p. 205. <http://dx.doi.org/10.1007/1-84628-493-7>.
- Choma Bex, C., Carlier, C., Fur, A., Pinon, G., Germain, G., Rivoalen, E., 2020. A stochastic method to account for the ambient turbulence in Lagrangian vortex computations. *Appl. Math. Model.* 88, 38–54. <http://dx.doi.org/10.1016/j.apm.2020.05.025>.
- DNV GL, 2017. *Definitions of Availability Terms for the Wind Industry*. Technical Report August.
- Endo, T., Mitsunaga, K., Takahashi, K., Kobayashi, K., Matsuishi, M., 1974. Damage evaluation of metals for random or varying loading—three aspects of rain flow method. *Mech. Behav. Mater.* 371–380.
- Freebury, G., Musial, W., 2000. Determining equivalent damage loading for full-scale wind turbine blade fatigue tests. In: 2000 ASME Wind Energy Symposium. (February), p. 12. <http://dx.doi.org/10.2514/6.2000-50>, URL <http://arc.aiaa.org/doi/abs/10.2514/6.2000-50>.
- Gaurier, B., Davies, P., Deuff, A., Germain, G., 2013. Flume tank characterization of marine current turbine blade behaviour under current and wave loading. *Renew. Energy* 59, 1–12. <http://dx.doi.org/10.1016/j.renene.2013.02.026>.
- Guo, Q., Zhou, L., Wang, Z., 2015. Comparison of BEM-CFD and full rotor geometry simulations for the performance and flow field of a marine current turbine. *Renew. Energy* 75, 640–648. <http://dx.doi.org/10.1016/j.renene.2014.10.047>, URL <http://dx.doi.org/10.1016/j.renene.2014.10.047>.
- Harvey, S.W.T., Chen, X., Rowe, D., Bhavsar, K., Allsop, T., Gilbert, J., Stallard, T., Vogel, C.R., Willden, R.H.J., 2021. Tidal turbine benchmarking exercise: Geometry specification and environmental characterisation. In: *Proceedings of the 14th European Wave and Tidal Energy Conference*, 5–9th Sept 2021, Plymouth, UK.
- IMEchE, 2020. MeyGen tidal-energy array exports electricity of whole of 2019. *Professional Eng.* <https://www.imeche.org/news/news-article/world27s-largest-tidal-stream-array-has-record-201>.
- Jarrin, N., Benhamadouche, S., Laurence, D., Prosser, R., 2006. A synthetic-eddy-method for generating inflow conditions for large-eddy simulations. *Int. J. Heat Fluid Flow* 27 (4), 585–593. <http://dx.doi.org/10.1016/j.ijheatfluidflow.2006.02.006>.
- Kolmogorov, A.A.N., Mathematical, S.P., Sciences, P., 1991. The local structure of turbulence in incompressible viscous fluid for very large Reynolds numbers. *Proc. R. Soc. Lond. Ser. A* 434 (1890), 9–13. <http://dx.doi.org/10.1098/rspa.1991.0075>.
- Lande-Sudall, D., Stallard, T., Stansby, P., 2018. Co-located offshore wind and tidal stream turbines: Assessment of energy yield and loading. *Renew. Energy* 118, 627–643. <http://dx.doi.org/10.1016/j.renene.2017.10.063>.
- Martinat, G., Braza, M., Hoarau, Y., Harra, G., 2008. Turbulence modelling of the flow past a pitching NACA0012 airfoil at 105 and 106 Reynolds numbers. *J. Fluids Struct.* 24 (8), 1294–1303. <http://dx.doi.org/10.1016/j.jfluidstructs.2008.08.002>.
- McCann, G.N., Rawlinson-smith, R.I., Argyriadis, K., 2007. Load simulation for tidal turbines using wind turbine experience. *GH Tidal Bladed (1870)*, 10.
- McNaughton, J., Billard, F., Revell, A., 2014. Turbulence modelling of low Reynolds number flow effects around a vertical axis turbine at a range of tip-speed ratios. *J. Fluids Struct.* 47, 124–138. <http://dx.doi.org/10.1016/j.jfluidstructs.2013.12.014>.
- McNaughton, J., Harper, S., Sinclair, R., Sellar, B., 2015. Measuring and modelling the power curve of a commercial-scale tidal turbine. In: *Proceedings of 11th European Wave and Tidal Energy Conference*, Nantes, France, vol. 1. pp. 1–9. <http://dx.doi.org/10.1017/CBO9781107415324.004>, arXiv:arXiv:1011.1669v3.
- McNaughton, J., Rolfo, S., Apsley, D., Afgan, I., Stansby, P., Stallard, T., 2012. CFD prediction of turbulent flow on an experimental tidal stream turbine using RANS modelling. In: *1st Asian Wave and Tidal Conference Series*. <http://dx.doi.org/10.1017/CBO9781107415324.004>, arXiv:arXiv:1011.1669v3.
- Menter, F.R., 1994. Two-equation eddy-viscosity turbulence models for engineering applications. *AIAA J.* 32 (8), 1598–1605. <http://dx.doi.org/10.2514/3.12149>.
- Mullings, H., Stallard, T., 2018. Unsteady loading in a tidal array due to simulated turbulent onset flow. In: *3rd International Conference on Renewable Energies Offshore*.
- Mullings, H.R., Stallard, T., 2019. Assessment of tidal turbine load cycles using synthesised load spectra, including blade-scale fluctuations. In: *13th European Wave and Tidal Energy Conference*. pp. 1–9.
- Olcak, a., Stallard, T., Feng, T., Stansby, P.K., 2016. Comparison of a RANS blade element model for tidal turbine arrays with laboratory scale measurements of wake velocity and rotor thrust. *J. Fluids Struct.* 64, 87–106. <http://dx.doi.org/10.1016/j.jfluidstructs.2016.04.001>.
- Ouro, P., Harrold, M., Stoesser, T., Bromley, P., 2017. Hydrodynamic loadings on a horizontal axis tidal turbine prototype. *J. Fluids Struct.* 71, 78–95. <http://dx.doi.org/10.1016/j.jfluidstructs.2017.03.009>.
- Parkinson, S.G., Collier, W.J., 2016. Model validation of hydrodynamic loads and performance of a full-scale tidal turbine using Tidal Bladed. *Int. J. Mar. Energy* 16, 279–297. <http://dx.doi.org/10.1016/j.ijome.2016.08.001>.
- Payne, G.S., Stallard, T., Martinez, R., 2017. Design and manufacture of a bed supported tidal turbine model for blade and shaft load measurement in turbulent flow and waves. *Renew. Energy* 107, 312–326. <http://dx.doi.org/10.1016/j.renene.2017.01.068>, URL <http://linkinghub.elsevier.com/retrieve/pii/S0960148117300782>.
- Payne, G.S., Stallard, T., Martinez, R., Bruce, T., 2018. Variation of loads on a three-bladed horizontal axis tidal turbine with frequency and blade position. *J. Fluids Struct.* 83, 156–170. <http://dx.doi.org/10.1016/j.jfluidstructs.2018.08.010>.
- Scarlett, G., 2019. *Unsteady Hydrodynamics of Tidal Turbine Blades* (Ph.D. thesis).
- Sequeira, C.L., Miller, R.J., 2014. Unsteady gust response of tidal stream turbines. In: *2014 Oceans - St. John's, OCEANS 2014*. <http://dx.doi.org/10.1109/OCEANS.2014.7003026>.

- Slama, M., Pinon, G., El, C., Togneri, M., Gaurier, B., Germain, G., Facq, J.-v., Nuño, J., Mansilla, P., Nicolas, E., Marcille, J., Pacheco, A., 2021. Turbine design dependency to turbulence : An experimental study of three scaled tidal turbines. *Ocean Eng.* 234 (January), 109035. <http://dx.doi.org/10.1016/j.oceaneng.2021.109035>.
- Stallard, T., Collings, R., Feng, T., Whelan, J., 2013. Interactions between tidal turbine wakes: experimental study of a group of three-bladed rotors. *Phil. Trans. R. Soc. A* 371 (1985), 20120159. <http://dx.doi.org/10.1098/rsta.2012.0159>, URL <http://rsta.royalsocietypublishing.org/cgi/doi/10.1098/rsta.2012.0159>.
- Thies, P.R., Johanning, L., Karikari-Boateng, K.a., Ng, C., McKeever, P., 2015. Component reliability test approaches for marine renewable energy. *Proc. Inst. Mech. Eng. O* 229, 403–416. <http://dx.doi.org/10.1177/1748006X15580837>, URL <http://pio.sagepub.com/lookup/doi/10.1177/1748006X15580837>.
- Togneri, M., Masters, I., Orme, J., 2011. Incorporating turbulent inflow conditions in a blade element momentum model of tidal stream turbines. In: *Proceedings of the Twenty-First (2011) International Offshore and Polar Engineering Conference*, vol. 8. pp. 757–762.
- Togneri, M., Pinon, G., Carlier, C., Choma Bex, C., Masters, I., 2020. Comparison of synthetic turbulence approaches for blade element momentum theory prediction of tidal turbine performance and loads. *Renew. Energy* 145, 408–418. <http://dx.doi.org/10.1016/j.renene.2019.05.110>.
- Walker, S.R.J., Thies, P.R., 2021. Failure and reliability growth in tidal stream turbine deployments. In: *Proceedings of the 14th European Wave and Tidal Energy Conference*, 5-9th Sept 2021, Plymouth, UK.
- Weller, S.D., Parish, D., Gordelier, T., Para, B.D.M., Garcia, E.A., Goodwin, P., Tornroos, D., 2017. Open sea OWC motions and mooring loads monitoring at BiMEP. In: *12th European Wave and Tidal Energy Conference*. pp. 1–9.
- Weller, S.D., Thies, P.R., Gordelier, T., Johanning, L., 2015. Reducing reliability uncertainties for marine renewable energy. *J. Mar. Sci. Eng.* 3, 1349–1361. <http://dx.doi.org/10.3390/jmse3041349>.
- Wimshurst, A., Willden, R., 2018. Spanwise flow corrections for tidal turbines. *Int. Mar. Energy J.* 1 (2), 111–121.